Hindawi
International Journal of Aerospace Engineering
Volume 2022, Article ID 7153667, 16 pages
https://doi.org/10.1155/2022/7153667

Research Article

Autonomous Phase Control Combining EKF and Adaptive Neural Network for Remote Sensing Satellites

Xin Wang[1], **Guogang Wang**[2] **and Hongru Zheng**[3]

[1]*School of Petrochemical Technology, Jilin Institute of Chemical Technology, Jilin City 132022, China*
[2]*School of Information and Control Engineering, Jilin Institute of Chemical Technology, Jilin City 132022, China*
[3]*Laboratory of Attitude and Orbit Control, Chang Guang Satellite Technology CO.LTD, Changchun City 130012, China*

Correspondence should be addressed to Xin Wang; wangxin1990090@126.com and Guogang Wang; wang_guo_g@sina.com

Received 11 November 2021; Revised 2 March 2022; Accepted 18 March 2022; Published 12 April 2022

Academic Editor: Franco Bernelli-Zazzera

In this paper, a novel, effective, and feasible autonomous phase control algorithm based on the extended Kalman filtering (EKF) and neural network is firstly developed for addressing the problems of configuration maintenance of remote sensing satellite constellation. A balanced moment arm optimization method is employed to design the installation structure layout of the chemical propulsion system in the satellite. On that basis, an autonomous orbit control strategy is presented for controlling the phase of satellites, and the EKF algorithm is utilized to determine the orbit used to calculate the satellite phase. A radial basis function (RBF) neural network-based attitude control method is proposed to solve the attitude disturbance problem in the course of the phase control, and the RBF neural network is utilized to approximate the coupling torque of the orbit control. The simulation results demonstrate the feasibility of the designed automatic phase control strategy of the satellite.

1. Introduction

With the rapid development of commercial earth-observation satellites, some application requirements such as rapid revisit and coverage have been improved, while a single satellite could not meet these requirements. Therefore, satellite networks like Jilin-1 constellation, Zhuhai-1 constellation, OneWeb constellation, and Aleph constellation have been established by many commercial satellite companies. At present, the orbit control of satellite networks is entirely dependent on control instructions sent from the ground stations, increasing the burden of daily ground operation and the ground station pressure [1]. The ground station fails can affect the processing capacity of the satellite network. This clarifies the importance of autonomous orbit control of satellite networks. Although continuous tracking of the satellite by the ground monitoring and control network is unnecessary, a few data transceiver stations should be established to complete the uplink and downlink data transmission. Therefore, autonomous orbit control provides various advantages, including human investment saving and the flexibility improvement of space tasks [2].

There are lots of satellites in the orbit, such as earth-observation satellite [3, 4], global navigation satellite [5, 6], and communication satellite [7, 8]; the orbit control of these satellites includes orbit maintenance, phase adjusting, phase maintenance, position keeping, and local time maintenance of descending node. The preparatory work of orbit control includes orbit determination, orbit control strategy, orbit maneuver command processing, and operation execution. These frequent maneuvers may become burdensome for daily ground operations. Various studies have been devoted to autonomous orbit control. In the early days, the GPS receiver introduction leads to several theoretical works on autonomous orbit control of LEO satellites [9], in which its feasibility has been further verified by Plam et al. [10] and Gaias and Ardaens [11]. A ground-based autonomous orbit control strategy has been proposed by Christian et al. [12]

and successfully applied to TerraSAR-X with a special computing software to perform orbit control tasks. Although the mentioned strategy successfully solved the burden of daily ground operations, there are limited resources in the ground station of an extensive satellite network to meet frequent satellite operations requirements. Thus, an onboard autonomous orbit control strategy has been presented by Bolandi and Abrehdari [13], Florio et al. [14], Garulli et al. [15], De Florio et al. [16], and Zhong and Gurfil [17]. The autonomous orbit control of low-orbit satellite includes orbit determination, orbit, and attitude control.

In terms of orbit determination, least squares and Kalman filter methods are the most common methods. Since the Kalman filtering algorithm does not require historical observation data and a large amount of computation, it has been widely utilized in real-time processing systems. In Kalman filtering, both the system state and measurement equations should be linear, and the dynamic and observed noises should be zero-mean Gaussian white noise sequences. However, the orbit motion and GPS observation equations are highly nonlinear equations. Thus, the improved versions of the Kalman filter algorithm have been employed in the literature to determine the real-time orbit. Li and Xu [18] employed the onboard image of the regular-shaped object to design an orbit determination method. The 3D reconstruction method has been adopted to measure the object center's visual axis vector, while the EKF algorithm has been utilized to estimate the orbit parameters. Zhai et al. [19] adopted Lagrangian multiplier techniques to develop a novel constrained Kalman filter framework for autonomous orbit determination. Jiang et al. [20] employed the reduction dynamic EKF to construct an improved GPS+BeiDou system (BDS) combination model and utilized the orbital dynamics model and EKF algorithm for smoothing the global navigation satellite system (GNSS) positioning results to improve the orbit accuracy. The Newton-Raphson method (NRM), combined with the EKF algorithm, named the NRM/EKF method, has been employed to present an orbit determination method for low-earth orbit satellites. Rough position values calculated in the NRM pre-processing step were provided as measurement inputs to the EKF algorithm to estimate the satellite's position and velocity vector [21]. Sun et al. [22] employed the random model, measurement equation, and model structure of orbit motion for filtering design and proposed an enhanced EKF to deal with unknown significant measurement deviations. A real-time high-precision orbit determination has been successfully realized using the improved Kalman filter algorithm in the above studies. Thus, the Kalman filter algorithm is appropriate to determine the orbit in real-time.

In terms of orbit and attitude control, due to a large deviation of the propulsion system, the satellite attitude will be greatly disturbed in the orbit control process, resulting in flywheel saturation. Therefore, it is necessary to adopt the propulsion system for attitude control. A thrusters-based attitude control method has been proposed for autonomous orbit control by Sato et al. [23], employing a low-thrust, 4-nozzle propulsion system and a pre-calculated thruster selection table for optimizing thrust and torque to achieve effective orbit control and maintain high-precision attitude stability for a long time. Gao et al. [24] combined autonomous orbit determination with autonomous control to present an integrated design method in which the neural network state observer has been designed to estimate the inter-satellite ranging information, and the controller has been constructed autonomously by another neural network based on the estimated state and the predefined correction trajectory. Bock and Tajmar [25] adopted a self-developed electric propulsion system to realize orbit and two-axis attitude control. The propulsion system can provide a large control torque suitable for the control system with a large disturbance torque. Yang and Liu [26] proposed a RBF neural network-based control algorithm to solve the unknown external disturbance problem for the satellite system. Cheng and Shu [27] combined the neural network with a genetic algorithm to estimate the unknown parameters of the satellite system. However, the neural network is a slow algorithm. Sliding mode control has been widely utilized in many fields due to its advantages, such as its simple algorithm, fast response, and strong robustness [28]. Asadi and Bagherzadeh [29] proposed a sliding mode control approach for nonlinear uncertain systems with external disturbances. The sliding mode control has been utilized to solve the spacecraft attitude stabilization problem in the presence of unknown external disturbances [30]. The mentioned problems have been solved through sliding mode control and neural networks. Therefore, the autonomous phase control using EKF and adaptive neural network is an effective method for low-orbit satellite constellation maintenance.

Finally, the essential contributions of this paper can be summarized as follows:

(1) In order to get the reasonable torque in the three directions, the structural layout of the chemical propulsion system is optimized by using the balanced force arm optimization method

(2) The EKF algorithm is utilized to determine the orbit used to calculate the satellite phase, and an autonomous orbit control strategy is designed for controlling the satellite phase

(3) A RBF neural network-based attitude control method is presented to solve the attitude disturbance problem in the course of the phase control, and the RBF neural network is employed to approximate the coupling torque of the orbit control. Simulation results show the effectiveness of the proposed algorithm. Compared to the PD control method, the proposed control strategy eliminates the influence of coupling torque and improves the attitude control accuracy

This paper is organized as follows. The propulsion system's structure layout and the model of the orbit and attitude dynamics are introduced in Section 2. This is followed by designing an autonomous phase control algorithm in Section 3, including EKF design, autonomous orbit control

algorithm, and attitude control algorithm. The autonomous orbit control strategy associated with a comparison with different control strategies is presented in Section 4. Finally, conclusions are provided in Section 5.

2. Dynamics Model

The satellite orbit control is subject not only to various perturbation forces but also to the thrust of the propulsion system. Similarly, the satellite attitude depends on the effect of the coupling torque. Hence, this section models the orbital dynamics, propulsion system layout, and attitude dynamics, respectively.

2.1. Orbit Dynamics Model. Since the satellite is in a synchronous solar orbit of 500~1000 km, the atmospheric influence should be considered. The orbital dynamics model [31] is obtained as

$$(M_0\text{-}M)\ddot{\mathbf{R}} = \mathbf{F}_c + \mathbf{F}_a + \mathbf{F}_s + \mathbf{F}_g. \tag{1}$$

$$M = \frac{\mathrm{Ft}_1}{I_s}, \tag{2}$$

where $\mathbf{R} = [x \quad y \quad z]^{\mathrm{T}}$ is the position vector of the satellite, M_0 is the initial mass of the satellite, M is the mass of fuel consumption, F is the thrust provided by each thruster, t_1 is the working time of the orbit-controlled thruster, I_s is vacuum specific impulse, $\mathbf{F}_a$ is the atmospheric perturbation force, $\mathbf{F}_s$ is the solar pressure, $\mathbf{F}_g$ is the gravity gradient, and $\mathbf{F}_c$ is the control force of the propulsion system.

2.2. Structure Layout of Propulsion System. The chemical propulsion system consists of five thrusters; one thruster is utilized for orbit control, while the others are employed for an attitude adjustment. The body coordinate system is denoted by $O-XYZ$. The attitude-controlled thruster is installed symmetrically on the X and Y axes of the satellite, while the geometric axis of the orbit-controlled thruster passes through the mass center. In order to make each attitude-controlled thruster of the propulsion system generate torque in three directions and better adjust the attitude of the satellite, an inclination angle is designed when the attitude-controlled thruster is installed. This optimal inclination angle is selected according to the method and the principles in the Appendix, and the inclination angle of the attitude-controlled thruster is -20°, as shown in Figure 1. The installation structure of the chemical propulsion system is successfully applied to an in-orbit satellite. According to the above structure model, the triaxial torque of ith thruster acting on the satellite coordinate system can be described as

$$\begin{cases} T_{ix} = F|L_a \cos(\theta)| \\ T_{iy} = F|-L_b \cos(\theta) + L_c \sin(\theta)|, i = 1, 2, 3, 4, \\ T_{iz} = F|L_c \sin(\theta)| \end{cases} \tag{3}$$

where L_a and L_b are, respectively, the distances from each thruster to the X and Y axes, L_c is the projected distance from each thruster to the mass center, F is the chemical propulsion thrust, and θ is the inclination angle of the attitude-controlled thruster.

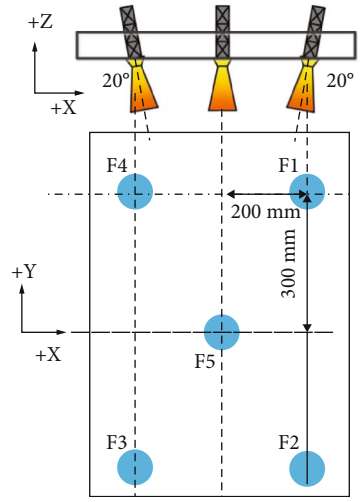

Figure 1: Diagram of propulsion system structure.

2.3. Attitude Dynamics Model. Defining attitude quaternion $\mathbf{q} = [q_1\ q_2\ q_3\ q_4]^T$. The kinematics and dynamics equations of the satellite can be written as

$$\begin{cases} \dot{\mathbf{q}} = \dfrac{1}{2}\mathbf{B}\mathbf{w} \\ \mathbf{I}\dot{\mathbf{w}} + \mathbf{w} \times \mathbf{I}\mathbf{w} + \boldsymbol{\tau}_d = \boldsymbol{\tau} \end{cases}. \tag{4}$$

where $\mathbf{B} = [\mathbf{q}_1 \quad \mathbf{q}_2 \quad \mathbf{q}_3 \quad \mathbf{q}_4]^T$, $\mathbf{q}_1 = [q_4 \quad q_3 \quad q_2 \quad -q_1]^T$, $\mathbf{q}_2 = [-q_3 \quad q_4 \quad q_1 \quad -q_2]^T$, $\mathbf{q}_3 = [q_2 \quad -q_1 \quad q_4 \quad -q_3]^T$, $\mathbf{q}_4 = [q_1 \quad q_2 \quad q_3 \quad q_4]^T$, $\mathbf{I}$ is the moment of inertia, $\mathbf{w}$ is the angular velocity of the satellite in the inertial system, $\boldsymbol{\tau}$ is the control torque of the satellite, and $\boldsymbol{\tau}_d$ is the interference torque of the chemical propulsion system. Since it is difficult to obtain an accurate system deviation from the measuring parts, the adaptive controller is designed to compensate for the uncertainties, while the sliding mode control will be utilized to improve the stability and robustness of the control system.

3. Autonomous Phase Control Algorithm Design

Autonomous phase control includes filter design, autonomous orbit control algorithm design, and attitude control design in the process of orbit control, as shown in Figure 2.

3.1. EKF Design. Considering the central gravitation term, and higher order term J_2, J_3, and J_4, the gravity potential function of the earth is

$$U = \frac{\mu}{R}\left\{1 - \frac{J_2 R_e^2}{2R^2}\left(3\sin^2(\varphi) - 1\right) - \frac{J_3 R_e^3}{2R^3}\left(5\sin^3(\varphi) - 3\sin(\varphi)\right) - \frac{J_4 R_e^4}{8R^4}\left(35\sin^4(\varphi) - 30\sin^2(\varphi) + 3\right)\right\} + W_g, \tag{5}$$

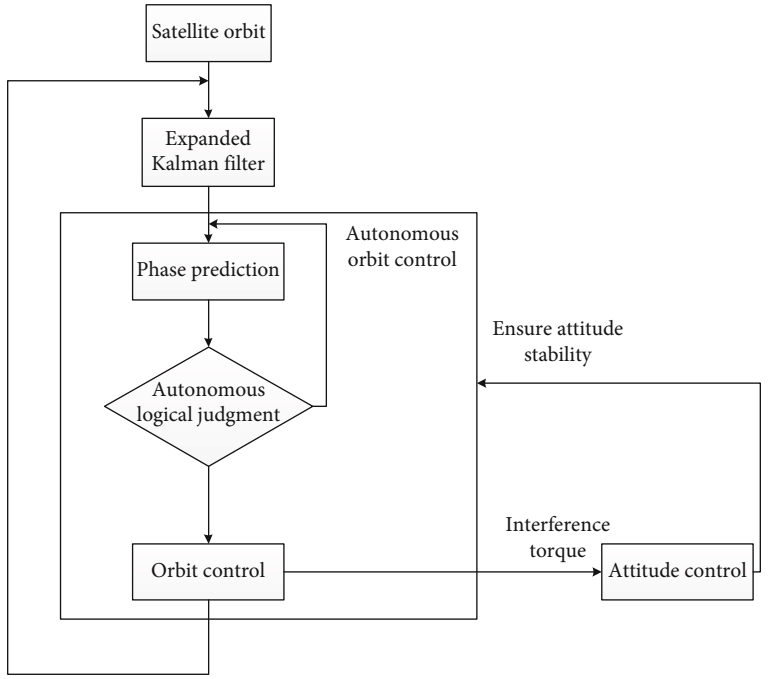

Figure 2: The flow chart of autonomous phase control.

where R_e is the earth radius, μ is the gravitational constant, φ is the geocentric latitude, $\varphi = \arcsin z/R$, $R = |\mathbf{R}|$ is the orbital position module, and W_g is the higher order uncertainties.

The motion of the satellite can be formulated as

$$\frac{d^2x}{dt^2} = -\frac{\mu x}{R^3}\left\{1 + \frac{3J_2R_e^2}{2R^2}\left(1 - \frac{5z^2}{R^2}\right) + \frac{5J_3R_e^3}{2R^3}\left(\frac{3z}{R} - \frac{7z^3}{R^3}\right) - \frac{5J_4R_e^4}{8R^4}\left(3 - \frac{42z^2}{R^2} + \frac{63z^4}{R^4}\right)\right\} + W_x, \tag{6}$$

$$\frac{d^2y}{dt^2} = \frac{\partial U}{\partial y} = \frac{d^2x}{dt^2}\frac{y}{x} + W_y, \tag{7}$$

$$\frac{d^2z}{dt^2} = -\frac{\mu z}{R^3}\left\{1 + \frac{3J_2R_e^2}{2R^2}\left(3 - \frac{5z^2}{R^2}\right) + \frac{5J_3R_e^3}{2R^3} \cdot \left(\frac{6z}{R} - \frac{7z^3}{R^3} - \frac{3R}{5z}\right) - \frac{5J_4R_e^4}{8R^4}\left(15 - \frac{70z^2}{R^2} + \frac{63z^4}{R^4}\right)\right\} + W_z, \tag{8}$$

where $\begin{bmatrix} W_x & W_y & W_z \end{bmatrix}^T = \begin{bmatrix} \partial W_g/\partial x & \partial W_g/\partial y & \partial W_g/\partial z \end{bmatrix}^T$ is model uncertainties. Consider that the satellite velocity vector is denoted by $\mathbf{V} = \begin{bmatrix} v_x & v_y & v_z \end{bmatrix}^T$, while the state variable of the determined orbit state filter is represented by $\mathbf{X} = [x \quad y \quad z \quad v_x \quad v_y \quad v_z]^T$. Now, the state and observation equations of the satellite orbit can be obtained as

$$\begin{cases} \dot{\mathbf{X}} = \mathbf{F}[\mathbf{X}, t] + \mathbf{W}(t) \\ \mathbf{Z} = \mathbf{H}(\mathbf{X}, t) + \mathbf{V}(t) \end{cases}, \tag{9}$$

where $W = \begin{bmatrix} 0 & 0 & 0 & W_x & W_y & W_z \end{bmatrix}^{\mathrm{T}}$, $\mathbf{v}(t)$ is the measurement noise, and $\mathbf{H}(\mathbf{X}, t)$ and $\mathbf{F}[\mathbf{X}, t]$ are the vector function, $\mathbf{F}(\mathbf{X}, t) = \begin{bmatrix} F_1 & F_2 & F_3 & F_4 & F_5 & F_6 \end{bmatrix}^T$, which can be described as

$$\begin{cases} F_1 = v_x, F_2 = v_y, F_3 = v_z \\ F_4 = \dfrac{d^2x}{dt^2}, F_5 = \dfrac{d^2y}{dt^2}, F_6 = \dfrac{d^2z}{dt^2} \end{cases}. \tag{10}$$

After linearizing and discretizing Equation (9), we have

$$\begin{cases} \mathbf{X}_k = \mathbf{A}\mathbf{X}_{k-1} + \mathbf{W}_k \\ \mathbf{Z}_k = \mathbf{H}_k\mathbf{X}_k + \mathbf{V}_k \end{cases}, \tag{11}$$

where $\mathbf{W}_k$ and $\mathbf{V}_k$ are independent Gaussian white noise with zero mean, $E = \mathbf{W}_k\mathbf{W}_j^T = \mathbf{Q}_k\boldsymbol{\delta}_{kj}$, and $E = \mathbf{V}_k\mathbf{V}_j^T = \mathbf{R}_k\boldsymbol{\delta}_{kj}$, in which $\mathbf{Q}_k$ and $\mathbf{R}_k$ are the covariance of Gaussian white noises. Here, the matrix $\mathbf{A}$ is given by

$$\mathbf{A} = \frac{\partial \mathbf{F}(\mathbf{X}, t)}{\partial \mathbf{X}} = \begin{bmatrix} 0 & 0 & 0 & 1 & 0 & 0 \\ 0 & 0 & 0 & 0 & 1 & 0 \\ 0 & 0 & 0 & 0 & 0 & 1 \\ \dfrac{\partial F_4}{\partial x} & \dfrac{\partial F_4}{\partial y} & \dfrac{\partial F_4}{\partial z} & 0 & 0 & 0 \\ \dfrac{\partial F_5}{\partial x} & \dfrac{\partial F_5}{\partial y} & \dfrac{\partial F_5}{\partial z} & 0 & 0 & 0 \\ \dfrac{\partial F_6}{\partial x} & \dfrac{\partial F_6}{\partial y} & \dfrac{\partial F_6}{\partial z} & 0 & 0 & 0 \end{bmatrix}. \tag{12}$$

The state transition matrix can be calculated as

$$\mathbf{\Phi}_{k,k-1} = \mathbf{I}_{6\times6} + \mathbf{A}T + \mathbf{A}^2T^2/2 + \cdots + \mathbf{A}^kT^k/k! + \cdots \tag{13}$$

where $\mathbf{I}_{6\times6}$ is the identity matrix, and T is the sampling period.

The observation matrix $\mathbf{H}_k$ is described as

$$\mathbf{H}_k = \frac{\partial \mathbf{H}(\mathbf{X}, t)}{\partial \mathbf{X}} = \left[\frac{\partial \mathbf{H}(\mathbf{X}, t)}{\partial \mathbf{R}} \frac{\partial \mathbf{H}(\mathbf{X}, t)}{\partial \mathbf{V}}\right]. \tag{14}$$

Then, the EKF equation can be expressed as

$$\begin{cases} \hat{\mathbf{X}}_{k/k-1} = \hat{\mathbf{X}}_{k-1} + F\left[\hat{\mathbf{X}}_{k-1}, t_{k-1}\right]T \\ \mathbf{P}_{k/k-1} = \mathbf{\Phi}_{k/k-1}\mathbf{P}_{k-1}\mathbf{\Phi}_{k/k-1}^T + \mathbf{Q}_k \\ \mathbf{K}_k = \mathbf{P}_{k/k-1}\mathbf{H}_k^T\left[\mathbf{H}_k\mathbf{P}_{k/k-1}\mathbf{H}_k^T + \mathbf{R}_k\right]^{-1} \\ \delta\hat{\mathbf{X}}_k = \mathbf{K}_k\left\{\mathbf{Z}_k - \mathbf{H}\left[\hat{\mathbf{X}}_{k/k-1}, k\right]\right\} \\ \mathbf{P}_k = (\mathbf{I} - \mathbf{K}_k\mathbf{H}_k)\mathbf{P}_{k/k-1}(\mathbf{I} - \mathbf{K}_k\mathbf{H}_k)^T + \mathbf{K}_k\mathbf{R}_k\mathbf{K}_k^T \\ \hat{\mathbf{X}}_k = \hat{\mathbf{X}}_{k/k-1} + \delta\hat{\mathbf{X}}_k \end{cases}, \tag{15}$$

where $\mathbf{P}_k$ is the state estimate covariance. Initialize $\hat{X}_0$, P_0, T, Q_k, R_k, the observed data $\mathbf{Z}_k$ is the system input. Recursion is carried out through formula (15) until the end. The algorithm description of EKF is shown as Figure 3. Equation (15) can be employed to determine the satellite position and velocity in real-time.

3.2. Autonomous Orbit Control Algorithm. For commercial Earth-observation constellation, the phase distribution maintenance is particularly essential for the revisit and coverage of satellites. If the altitude difference of two satellites in the same orbital plane is large, the phase will exceed a threshold within a few days. Therefore, two satellites should be kept in one orbital altitude as far as possible. The following assumptions are considered:

Assumption 1. A satellite can acquire orbit data from another satellite.

Assumption 2. The GPS navigation receiver data is usually available during orbit control.

Assumption 3. The deviation quaternion and angular velocity are continuous and bounded.

The orbital dynamics equation can be converted to a perturbation equation with six elements. The average semi-major axis of the satellite N_A and the satellite N_B are a_1 and a_2, respectively, with phase σ distributed in an orbital plane. Their phases should be kept within $\sigma \pm \delta$, while the orbital period difference ΔT is given by

Begin
Initial value $\hat{X}_0$, P_0, T, Q_k, R_k
For k = 1:1:n
Input measurement data Z_k
Calculate $A = \frac{\partial \mathbf{F}(\mathbf{X},t)}{\partial \mathbf{X}}$
$\mathbf{\Phi}_{k,k-1} = \mathbf{I}_{6\times6} + \mathbf{A}T + \mathbf{A}^2T^2/2 + \cdots + \mathbf{A}^kT^k/k! + \cdots$
$\hat{\mathbf{X}}_{k/k-1} = \hat{\mathbf{X}}_{k-1} + \mathrm{F}\left[\hat{\mathbf{X}}_{k-1}, t_{k-1}\right]T$
$\mathbf{P}_{k/k-1} = \mathbf{\Phi}_{k/k-1}\mathrm{P}_{k-1}\mathbf{\Phi}_{k/k-1}^T + \mathbf{Q}_k$
$\mathbf{K}_k = \mathbf{P}_{k/k-1}\mathbf{H}_k^T\left[\mathbf{H}_k\mathbf{P}_{k/k-1}\mathbf{H}_k^T + \mathbf{R}_k\right]$
$\delta\hat{\mathbf{X}}_k = \mathbf{K}_k\left\{\mathbf{Z}_k - \mathbf{H}\left[\hat{\mathbf{X}}_{k/k-1}, k\right]\right\}$
$\mathbf{P}_k = (\mathbf{I} - \mathbf{K}_k\mathbf{H}_k)\mathbf{P}_{k/k-1}(\mathbf{I} - \mathbf{K}_k\mathbf{H}_k) + \mathbf{K} - \mathrm{R}_k\mathbf{K}_k^T$
$\hat{\mathbf{X}}_k = \hat{\mathbf{X}}_{k/k-1} + \delta\hat{\mathbf{X}}_k$
end

Figure 3: The structure of EKF.

$$\frac{\Delta T}{2\pi} = \begin{cases} \sqrt{(a_1)^3/\mu} - \sqrt{(a_2)^3/\mu}, & \text{if} \quad a_1 > a_2 \\ \sqrt{(a_2)^3/\mu} - \sqrt{(a_1)^3/\mu}, & \text{if} \quad a_1 < a_2 \end{cases}. \tag{16}$$

where $2/|R| - V^2/\mu = 1/a$, $R = \mathrm{sqrt}(x^2 + y^2 + z^2)$, $V = \mathrm{sqrt}(v_x^2 + v_y^2 + v_z^2)$, where $\mathbf{X} = [x \quad y \quad z \quad v_x \quad v_y \quad v_z]^{\mathrm{T}}$ are obtained by formula (15). The phase shift of the two satellites is determined as

$$\varphi = \frac{\Delta T}{T_1^2} \times 360 \times T, \tag{17}$$

where $T_1 = 2\pi\sqrt{(a_1)^3/\mu}$.

Autonomous logical judgment strategy is given by

$$\Delta a = \begin{cases} -\lambda|a_1 - a_2|, & a_1 > a_2 \& \varphi > \delta \\ +\lambda|a_1 - a_2|, & a_1 \le a_2 \& \varphi > \delta \\ 0, & \varphi \le \delta \end{cases}, \tag{18}$$

where λ is the gain coefficient and δ is the phase limit of two satellites, The symbols + and – indicate the rise and fall of the orbit altitude of satellite N_A.

The semi-major axis change caused by orbital perturbation is obtained as

$$\begin{cases} \Delta a_1 = \dfrac{2}{n\sqrt{1-e^2}}\left[e(\Delta V_S \sin(f) + \Delta V_T \cos(f)) + \Delta V_T\right] \\ \Delta a_2 = \dfrac{2}{n\sqrt{1-e^2}}\Delta V_T \end{cases}, \tag{19}$$

where ΔV_S and ΔV_T are, respectively, the radial and lateral velocity increments provided by the orbit-controlled thruster, ΔV_T is the lateral velocity increment provided by the attitude-controlled thruster, n is the orbital angular velocity, $e(e \approx 0)$ is the eccentricity, and f is the true anomaly.

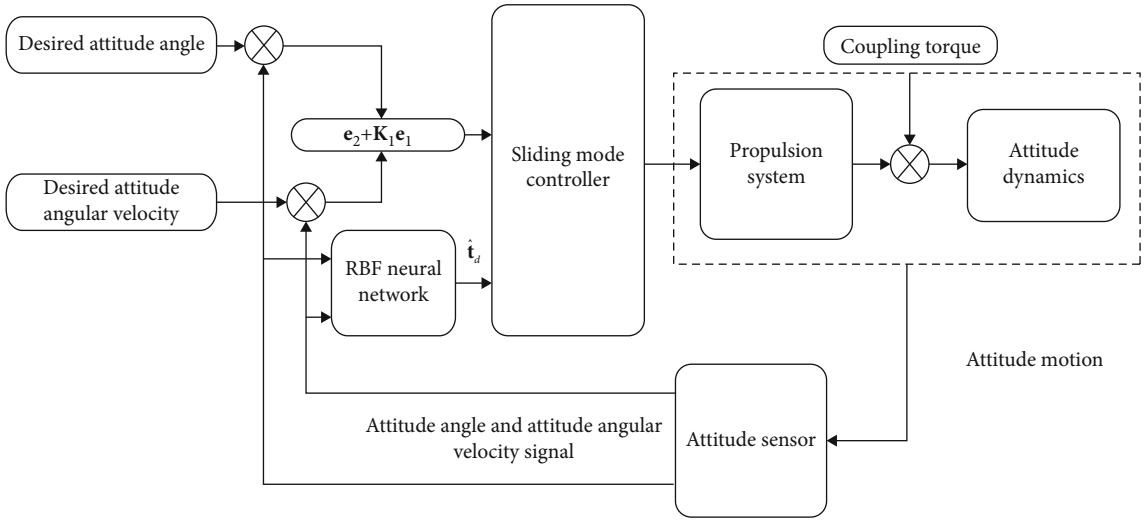

Figure 4: Diagram of the attitude control algorithm.

Table 1: Deviation parameters of the propulsion system.

Parameters	Values
Geometric installation deviation	$\theta_a = [0.5\,;0\,;0\,;0\,;0.5]^\circ$
Geometric installation deviation azimuth	$\theta_{ac} = [90\,;90\,;90\,;90\,;90]^\circ$
Thrust deflection	$\theta_b = [1\,;1\,;1\,;1\,;1]^\circ$
Thrust deflection azimuth	$\theta_{bc} = [90\,;90\,;90\,;90\,;90]^\circ$
Center of mass	$\mathbf{I}_{mc} = [0.01\,;0.01\,;0.01]$mm

Table 2: Initial orbit parameters.

Parameters	Initial orbit parameters
Position of x	-1897.1 km
Position of y	-6647.74 km
Position of z	3.13363 km
Velocity of v_x	-0.94481 km/s
Velocity of v_y	0.273174 km/s
Velocity of v_z	7.52935 km/s

Table 3: Initial parameters of the system.

Parameters	Value
Thrust	$F = 1.3$N
Proportion coefficient	$K_a = 1.3$
Satellite mass	M_0=200 kg
Vacuum specific impulse	I_S=2000 N · s/kg
Moment of inertia	$\mathbf{I}$ = diag (55 50 30)
Initial attitude quaternion	$\mathbf{q}_0 = [0.2\,;0.3\,;0.4]$
Initial attitude angular velocity	$\mathbf{w}_0 = [-0.2\,;0.1\,;0.3]$ (°/s)
Desired attitude quaternion	$\mathbf{q}_d = [0\,;0.8509\,;0]$
Desired attitude angular velocity	$\mathbf{w}_0 = [0\,;0\,;0]$ (°/s)

Then, the controller of the chemical propulsion system is given by

$$\Delta a = \Delta a_1 + \Delta a_2, \tag{20}$$

where $\Delta a_2 = K_a \Delta a_1$. K_a is the proportion coefficient of the attitude-controlled thruster, which should be calibrated after the satellite enters into the orbit.

The impulse control model is applied to the chemical propulsion system. Thus, the control time is allocated to calculate the velocity increment, and the lateral velocity increment provided by the thruster is obtained as

$$\begin{cases} \Delta V_T = \dfrac{\mathrm{Ft}_1}{M_0} \\ \Delta V_t = \dfrac{\mathrm{Ft}_2}{M_0} \end{cases}, \tag{21}$$

where $t_2 = \sum_{i=1}^{4} t_{2i}$ is the total working time of the attitude-controlled thruster acting on the lateral direction, and t_{2i} is the working time of each thruster acting on the lateral direction. During the working time t_2 of the propulsion system, there will be coupling torque $\boldsymbol{\tau}_d$ in the satellite attitude.

3.3. Attitude Control Algorithm during Orbit Control. In the orbit control process, due to the thrust direction deviation, thruster installation deviation, mass center deviation, and

other factors in the propulsion system, the orbit-controlled thrust will generate the attitude coupling torque to the satellite, leading to the satellite's attitude instability. Now, an orbit control algorithm is designed for the satellite system (3) and orbit dynamics model (1)~(2) to ensure attitude stability.

Consider that $\mathbf{q}_d$ is the desired attitude angle, and $\mathbf{w}_d = [w_{1d} \quad w_{2d} \quad w_{3d}]^T$ is the desired angular velocity. Now, the deviation quaternion $\mathbf{e}_1$ and the deviation angular velocity $\mathbf{e}_2$ can be calculated as

$$\begin{cases} \mathbf{e}_1 = \mathbf{q} \otimes \mathbf{q}_d \\ \mathbf{e}_2 = \mathbf{w} - \mathbf{w}_d \end{cases}. \tag{22}$$

The following sliding mode surface is appropriately defined to tend the deviation quaternion and deviation angular velocity to zero

$$\mathbf{S} = \mathbf{e}_2 + \mathbf{K}_1 \mathbf{e}_1 = \mathbf{w} - \mathbf{w}_r, \tag{23}$$

where $\mathbf{w}_r = \mathbf{w}_d - \mathbf{K}_1 \mathbf{e}_1$, when $\mathbf{S} \longrightarrow 0$, the deviation quaternion and deviation angular velocity tend to zero along the sliding mode surface.

The derivative of the sliding surface $\mathbf{S}$ is calculated as

$$\dot{\mathbf{S}} = \dot{\mathbf{w}} - \dot{\mathbf{w}}_r. \tag{24}$$

In the orbit control process, the uncertain disturbance part of the dynamic model is approximated using a neural network. Defining

$$\mathbf{t}_d(\mathbf{q}, \mathbf{w}, \mathbf{W}) = \mathbf{W}^T \boldsymbol{\varphi} + \boldsymbol{\varepsilon}, \tag{25}$$

where $\mathbf{W}$ is the neural network weight value, $\boldsymbol{\varphi}$ is the neural network basis function, and $\boldsymbol{\varepsilon}$ is the approximation error. The neural network weight is defined as

$$\mathbf{W} = \arg \min_{\widehat{\mathbf{W}} \in U} \left\{ \sup_{\mathbf{q}, \mathbf{w} \in D} \left| \widehat{\mathbf{t}}_d(\mathbf{q}, \mathbf{w}, \widehat{\mathbf{W}}) - \mathbf{t}_d(\mathbf{q}, \mathbf{w}, \mathbf{W}) \right| \right\}, \tag{26}$$

where U and D are the ranges of $\mathbf{q}$, $\mathbf{w}$, and $\widehat{\mathbf{W}}$, and $\widehat{\mathbf{t}}_d(\mathbf{q}, \mathbf{w}, \widehat{\mathbf{W}})$ is the estimated value of $\mathbf{t}_d(\mathbf{q}, \mathbf{w}, \mathbf{W})$. As shown in Figure 4, a neural network is employed to approximate the coupling torque $\boldsymbol{\tau}_d$ of the satellite. It can be expressed as

$$\widehat{\mathbf{t}}_d(\mathbf{q}, \mathbf{w}, \mathbf{W}) = \widehat{\mathbf{W}}^T \widehat{\boldsymbol{\varphi}} + \widehat{\boldsymbol{\varepsilon}}. \tag{27}$$

The estimated error is given by

$$\begin{aligned} \tilde{\mathbf{t}}_d = \mathbf{t}_d - \widehat{\mathbf{t}}_d &= \mathbf{W}^T \boldsymbol{\varphi} + \boldsymbol{\varepsilon} - \widehat{\mathbf{W}}^T \widehat{\boldsymbol{\varphi}} - \widehat{\boldsymbol{\varepsilon}} = \mathbf{W}^T \boldsymbol{\varphi} - \mathbf{W}^T \widehat{\boldsymbol{\varphi}} + \mathbf{W}^T \widehat{\boldsymbol{\varphi}} \\ &\quad - \widehat{\mathbf{W}}^T \widehat{\boldsymbol{\varphi}} + \boldsymbol{\varepsilon} - \widehat{\boldsymbol{\varepsilon}} = \mathbf{W}^T \tilde{\boldsymbol{\varphi}} + \tilde{\mathbf{W}}^T \widehat{\boldsymbol{\varphi}} + \tilde{\boldsymbol{\varepsilon}}, \end{aligned} \tag{28}$$

where $\tilde{\mathbf{W}} = \mathbf{W} - \widehat{\mathbf{W}}$, and $\tilde{\boldsymbol{\varphi}} = \boldsymbol{\varphi} - \widehat{\boldsymbol{\varphi}}$.

Table 4: EKF parameters.

Parameters	Value
$\mathbf{P}_{k0}$	diag (200 300 400 0.3 0.5 0.3)
$\mathbf{Q}_k$	diag (15 15 15 8 8 8) × 0.0001
$\mathbf{R}_k$	diag (600 600 600 0.06 0.06 0.06) × 10
T	0.125s

Table 5: RBF neural network control parameters.

Parameters	Value
$\mathbf{K}_1$	diag (0.63 0.63 0.63)
$\mathbf{K}_d$	diag (88.7 78.8 78.8) × 0.23
$\mathbf{K}_s$	diag (0.006 0.006 0.006)
$\boldsymbol{\Gamma}$	diag (4 4 4 4 4 4 4) × 100

The control law is defined as

$$\boldsymbol{\tau} = \mathbf{I}\dot{\mathbf{w}}_r + \mathbf{w} \times \mathbf{I}\mathbf{w} + \widehat{\mathbf{t}}_d - \mathbf{K}_d \mathbf{S} - \mathbf{K}_s \mathrm{sat}(\mathbf{S}), \tag{29}$$

where the saturation function $\mathrm{sat}(\mathbf{S})$ can be expressed as

$$\mathrm{sat}(\mathbf{S}) = \begin{cases} 1 & \mathbf{S}_i > \Delta_i \\ -1 & \mathbf{S}_i < -\Delta_i \\ \mathbf{S}_i / \Delta_i & |\mathbf{S}_i| \le \Delta_i \end{cases}, \tag{30}$$

where $\mathbf{S} = [S_1 \quad S_2 \quad S_3 \quad S_4 \quad S_5 \quad S_6]^T$, and $\Delta_i (i = 1, \cdots 6)$ are arbitrary known constants. The saturation function is employed to suppress the chattering phenomenon caused by repeated switching on the sliding mode surface during the convergence process.

Equation (29) can be rewritten with the following form, which is similar to Equation (4)

$$\mathbf{I}(\dot{\mathbf{w}} - \dot{\mathbf{w}}_r) + \mathbf{t}_d - \widehat{\mathbf{t}}_d + \mathbf{K}_d \mathbf{S} + \mathbf{K}_s \mathrm{sat}(\mathbf{S}) = 0. \tag{31}$$

According to relations (24), (28), and (Proof), we have

$$\mathbf{I}\dot{\mathbf{S}} = -\tilde{\mathbf{t}}_d - \mathbf{K}_d \mathbf{S} - \mathbf{K}_s \mathrm{sat}(\mathbf{S}) \tag{32}$$

Theorem. *For satellite system (4), consider that the system interference and the satellite's desired orbit and attitude are bounded. Now, if an adaptive attitude controller can be designed using Equations (29) and (30), then the tracking error is bounded, while the adaptation update law can be described as*

$$\dot{\widehat{\mathbf{W}}} = -\boldsymbol{\Gamma} \widehat{\boldsymbol{\varphi}} \mathbf{S}^T \tag{33}$$

where $\Gamma = \mathrm{diag}\{\Gamma_{ii}\} (i = 1, 2 \cdots 7)$, and $\Gamma > 0$. When $t \longrightarrow \infty$, and $\mathbf{S} \longrightarrow 0$, then $\mathbf{q} \longrightarrow \mathbf{q}_d$ and $\mathbf{w} \longrightarrow \mathbf{w}_d$. This means that the tracking error is bounded.

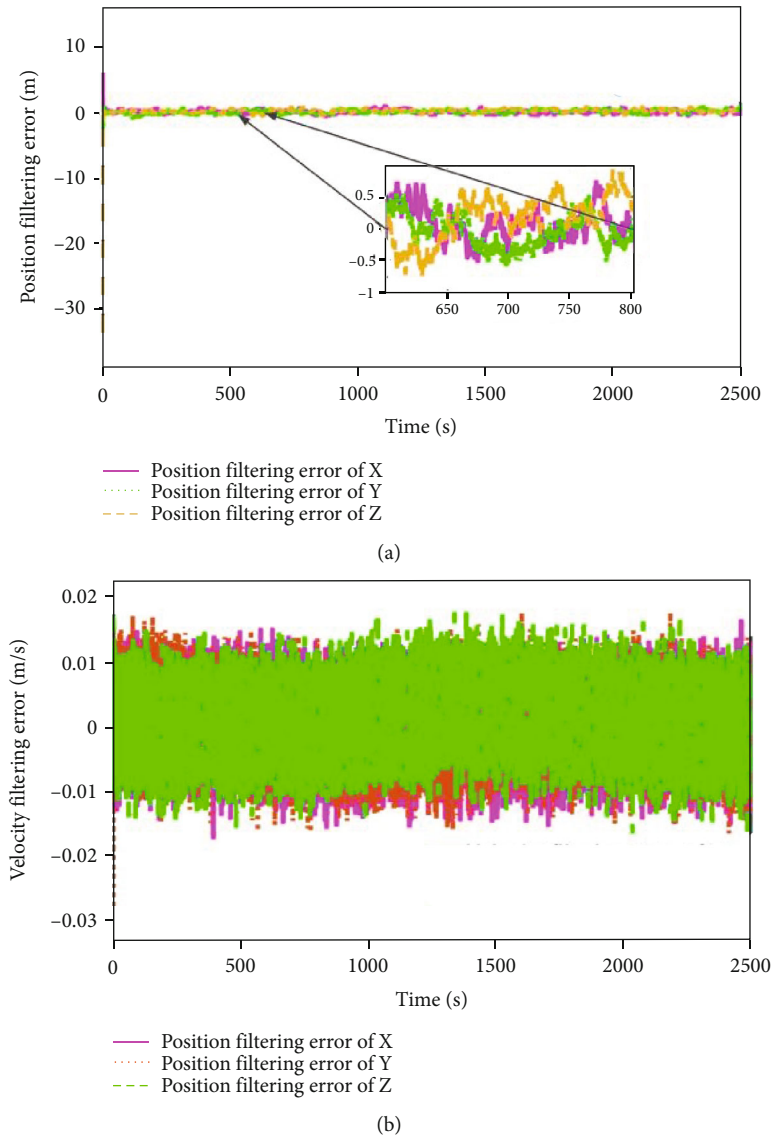

Figure 5: EKF algorithm effect. (a) The position error. (b) The velocity error.

Proof. Consider the following Lyapunov candidate function

$$V = \frac{1}{2}\mathbf{S}^T \mathrm{IS} + tr\left(\tilde{\mathbf{W}}^T \boldsymbol{\Gamma}^{-1} \tilde{\mathbf{W}}\right). \tag{34}$$

The time derivative of Equation (34) is calculated as

$$\begin{aligned} \dot{V} &= \mathbf{S}^T \mathbf{I}\dot{\mathbf{S}} + tr\left(\tilde{\mathbf{W}}^T \boldsymbol{\Gamma}^{-1} \dot{\tilde{\mathbf{W}}}\right) = \mathbf{S}^T\left(-\tilde{\mathbf{t}}_d - \mathbf{K}_d\mathbf{S} - \mathbf{K}_s \mathrm{sat}(\mathbf{S})\right) \\ &\quad + tr\left(\tilde{\mathbf{W}}^T \boldsymbol{\Gamma}^{-1} \dot{\tilde{\mathbf{W}}}\right) = -\mathbf{S}^T \mathbf{K}_d \mathbf{S} - \mathbf{S}\mathbf{K}_s \mathrm{sat}(\mathbf{S}) \\ &\quad - \mathbf{S}^T\left(\mathbf{W}^T \tilde{\boldsymbol{\varphi}} + \tilde{\mathbf{W}}^T \hat{\boldsymbol{\varphi}} + \tilde{\boldsymbol{\varepsilon}}\right) + tr\left(-\mathbf{W}^T \boldsymbol{\Gamma}^{-1} \dot{\hat{\mathbf{W}}}\right) \\ &= -\mathbf{S}^T \mathbf{K}_d \mathbf{S} - \mathbf{S}\mathbf{K}_s \mathrm{sat}(\mathbf{S}) - \mathbf{S}^T\left(\mathbf{W}^T \tilde{\boldsymbol{\varphi}} + \tilde{\boldsymbol{\varepsilon}}\right) \\ &\quad + tr\left(-\tilde{\mathbf{W}}^T\left(\boldsymbol{\Gamma}^{-1} \dot{\hat{\mathbf{W}}} + \hat{\boldsymbol{\varphi}}\mathbf{S}^T\right)\right) = -\mathbf{S}^T \mathbf{K}_d \mathbf{S} - \mathbf{S}\mathbf{K}_s \mathrm{sat}(\mathbf{S}) \\ &\quad - \mathbf{S}^T\left(\mathbf{W}^T \tilde{\boldsymbol{\varphi}} + \tilde{\boldsymbol{\varepsilon}}\right). \end{aligned} \tag{35}$$

□

If matrix $\mathbf{N}_{6\times6}$ is positive definite, $\|\mathbf{W}^T\tilde{\boldsymbol{\varphi}} + \tilde{\boldsymbol{\varepsilon}}\| \geq \|\mathbf{N}_{6\times6}\mathbf{S}\|$. Thus, we have

$$\left\|\mathbf{S}^T\right\| \cdot \left\|\mathbf{W}^T\tilde{\boldsymbol{\varphi}} + \tilde{\boldsymbol{\varepsilon}}\right\| \geq \left\|\mathbf{S}^T\right\| \cdot \|\mathbf{N}_{6\times6}\mathbf{S}\|. \tag{36}$$

The following inequalities are valid

$$\begin{cases} \left\|\mathbf{S}^T\right\| \cdot \left\|W^T\tilde{\varphi} + \tilde{\varepsilon}\right\| \geq \mathbf{S}^T\left(W^T\tilde{\varphi} + \tilde{\varepsilon}\right) \\ \left\|\mathbf{S}^T\right\| \cdot \|N_{6\times6}\mathbf{S}\| \geq \mathbf{S}^T(N_{6\times6}\mathbf{S}) \end{cases}. \tag{37}$$

Then when $\mathbf{S}^T(\mathbf{W}^T\tilde{\boldsymbol{\varphi}} + \tilde{\boldsymbol{\varepsilon}}) \geq \|\mathbf{S}^T\| \cdot \|\mathbf{N}_{6\times6}\mathbf{S}\|$, the following inequalities should be fulfilled

$$\mathbf{S}^T\left(W^T\tilde{\varphi} + \tilde{\varepsilon}\right) \geq \mathbf{S}^T(N_{6\times6}\mathbf{S}). \tag{38}$$

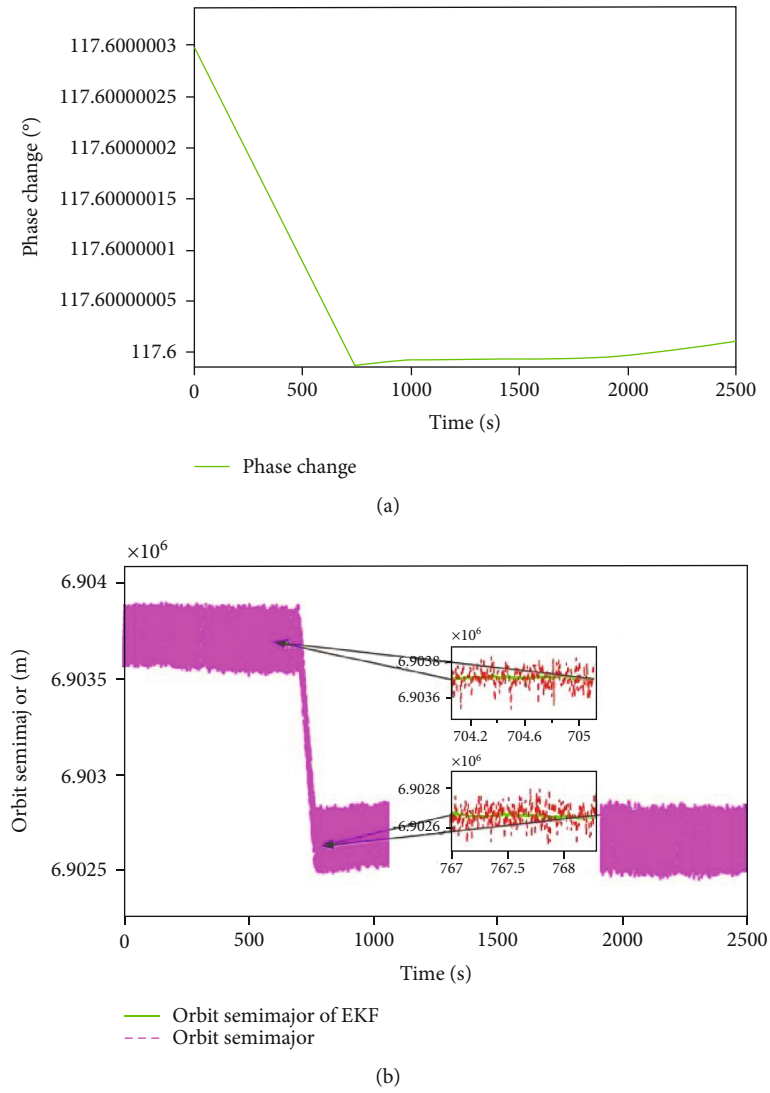

FIGURE 6: State change of the satellite. (a) The phase. (b) The orbit semi-major.

Thus, we have

$$\begin{aligned}\dot{V} &= -\mathbf{S}^T\mathbf{K}_d\mathbf{S} - \mathbf{S}\mathbf{K}_s\mathrm{sat}(\mathbf{S}) - \mathbf{S}^T\left(\mathbf{W}^T\tilde{\varphi} + \tilde{\varepsilon}\right) \\ &\leq -\mathbf{S}^T\mathbf{K}_d\mathbf{S} - \mathbf{S}\mathbf{K}_s\mathrm{sat}(\mathbf{S}) - \mathbf{S}^T\left(N_{6\times 6}\mathbf{S}\right) \leq 0.\end{aligned} \tag{39}$$

Case 1. If $\mathbf{S} = 0$, then $\dot{V} = 0$;

Case 2. If $\mathbf{S} \neq 0$, then $\dot{V} < 0$. According to the Lyapunov stability theory, the satellite control system of the satellite is bounded and stable.

Since $\mathbf{S}$ is uniformly continuous, integrable, and bounded as $t \longrightarrow \infty$, it is obtained by

$$\lim_{t\longrightarrow\infty} \mathbf{s} = 0. \tag{40}$$

Since $\mathbf{e}_1 \longrightarrow 0$ and $\mathbf{e}_2 \longrightarrow 0$, according to Barbalat Lemma, the system is asymptotically convergent, besides being stable.

4. Simulation Results and Discussion

In this section, a satellite with the chemical propulsion system of five thrusters is adopted to prove the validity of the proposed control method. The maximum control torque available is 0.5 Nm, where Table 1 shows the external input deviation of the propulsion model. The initial orbit and the system parameters as inputs are shown in Table 2 and Table 3, respectively. The EKF parameters are presented in Table 4.

Two attitude control algorithms, including the proportional-derivative (PD) control (which has been implemented) and the neural networks, are designed for the propulsion system to improve the attitude control accuracy. The PD controller parameters are chosen as $\mathbf{K}_p = \mathrm{diag}$

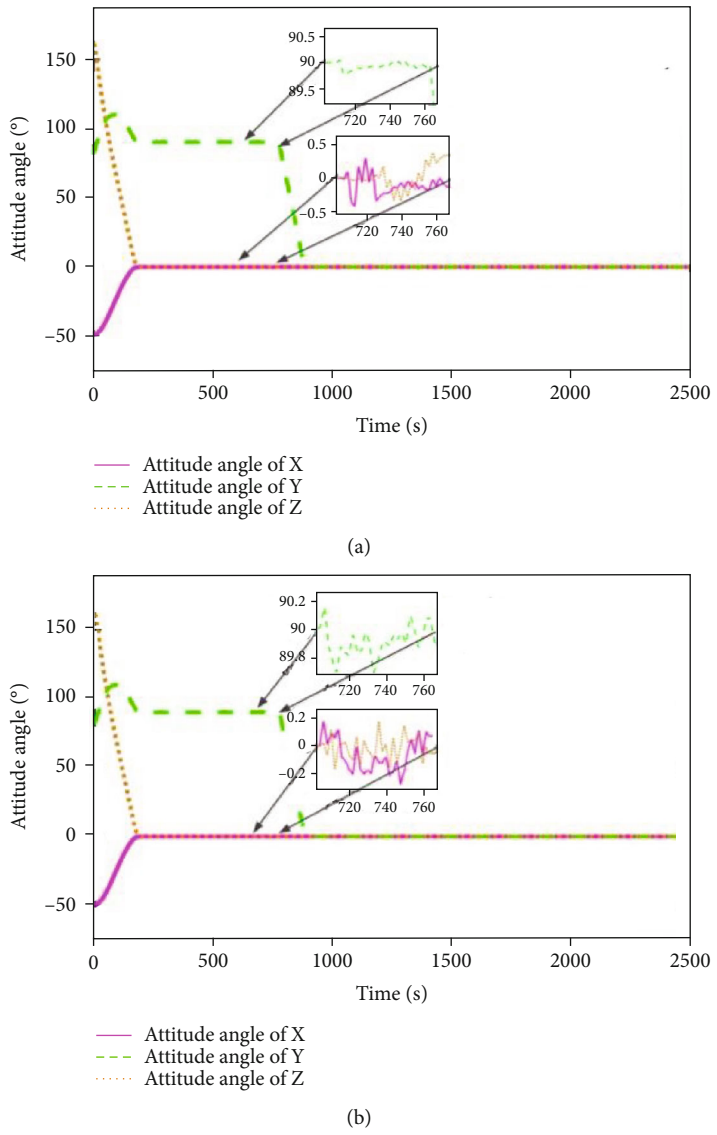

Figure 7: Attitude angle curve. (a) PD control. (b) RBF Neural network control.

$(27.5 \quad 25 \quad 15)$ and $\mathbf{K}_d = diag(137.5 \quad 125 \quad 75)$, and the RBF neural network parameters are listed in Table 5.

A three-layer neural network is employed to approximate the coupling torque of orbit control, while the hidden layer contains seven neurons. The radial basis function of the neural network is chosen as

$$\varphi_j = e^{\left(-\|X-c_j\|/2b_j^2\right)}, \quad j = 1, 2, \cdots 7, \tag{41}$$

where c_j and b_j are the center and width of the RBF neural network.

The inboard satellite orbit interfaces with actually random noises, making a large orbital instantaneous fluctuation. Thus, orbit filtering is required for the controller design. The random noises of orbit position and velocity in the system are in the range of [-30 30] and [-0.05 0.05], respectively. The designed EKF algorithm is employed to perform the orbit filtering of the satellite. The EKF effect is shown in Figure 5.

The following conclusions can be derived from the simulation results:

(1) Figures 5(a) and 5(b) show the error between the filtering position and the real position and the error between the filtering velocity and the real velocity, respectively. The solid, the colon, and the dotted lines in Figure 5(a) represent the position filtering errors of the X, Y, and Z axes, respectively. The solid, the colon, and the dotted lines in Figure 5(b) show the velocity filtering errors of the X, Y, and Z axes, respectively. Since the position data error of GPS on the satellite is about 30 m, which is not conducive to the strategy formulation of autonomous orbit

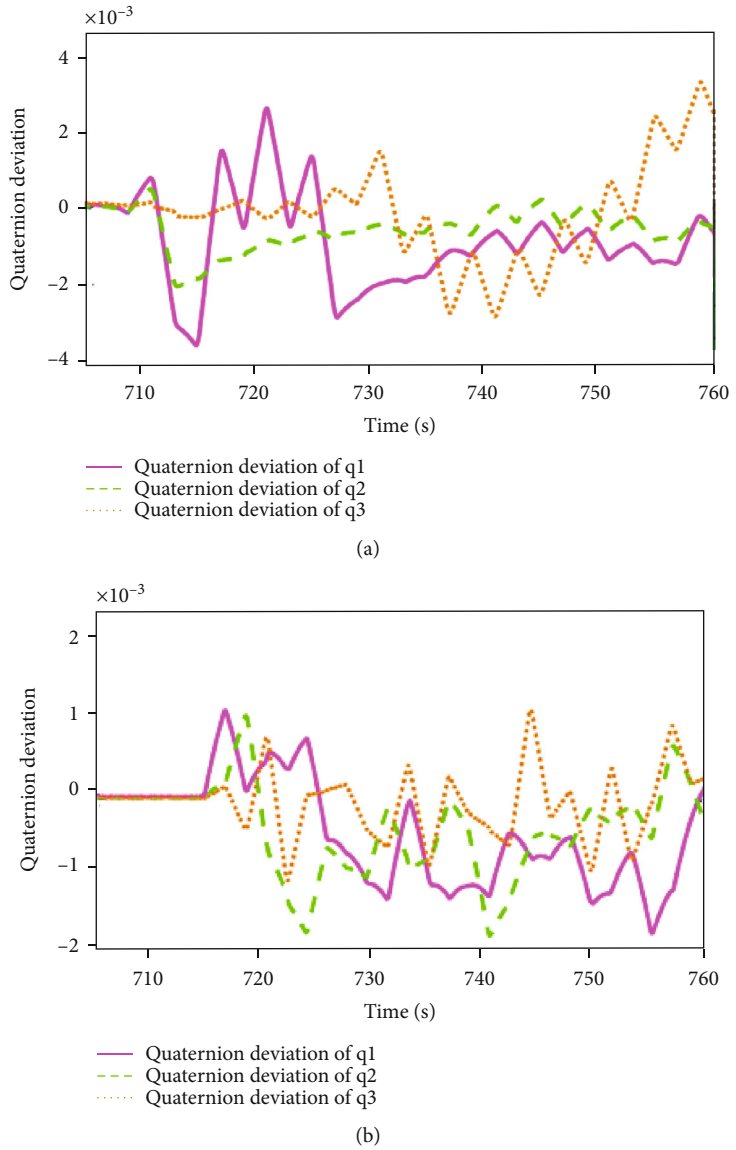

Figure 8: Quaternion deviation curve. (a) PD control. (b) Neural network sliding mode control.

control, the EKF algorithm is employed to filter the GPS data. The position noise is attenuated from the peak value of 30 m to within 0.6 m, while the velocity noise is attenuated from the peak value of 0.05 m/s to within 0.016 m/s. It can be seen that the designed EKF algorithm, which is successfully prepared for the formulation of an autonomous control strategy, can significantly improve the orbit determination accuracy

(2) Figures 6(a) and 6(b) show the phase change and the average orbit semi-major of the satellite, respectively. After the orbit is determined, the orbit control strategy will be calculated. The phase threshold is adjusted in the range of [117.5°-122.5°], and when the satellite phase exceeds this threshold, the satellite's propulsion system starts to work automatically. The orbit determination and phase tracking are necessary for autonomous phase maintenance. The average orbit semi-major is 6903.7 ± 0.2 km, the semi-major after applying the EKF algorithm is 6903.7 ± 0.02 km, and the orbital semi-major of the other satellite is 6902.7 ± 0.02 km. Therefore, the phase between the two satellites approaches at a certain speed (see Figure 6(a)), the phase between two satellites exceeds 117.5° at 705 s, the satellite autonomously develops the control strategy, the control time and duration are 705 s, and 62 s, respectively, and the control quantity of the semi-major is 1.04 km. In practice, more than 20 m should be in orbit to ensure that the satellite's orbit altitude is lower than that of another satellite. Since the orbit after applying the EKF algorithm has an instantaneous fluctuation of ±20 m, the control quantity is

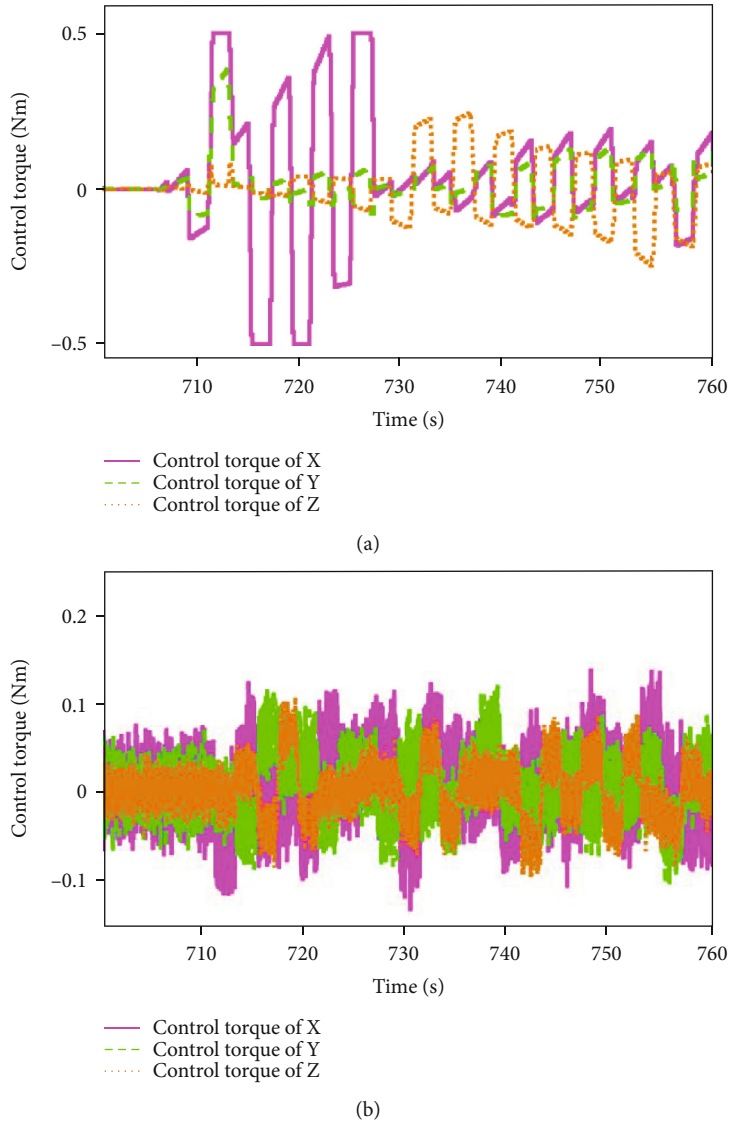

Figure 9: Control torque. (a) PD control. (b) Neural network sliding mode control.

increased by 40 m. It can be seen from Figure 6(b) that the satellite starts to control at 705 s, and stops control at 767 s, the orbit semi-major is reduced from 6903.7 ± 0.02 km to 6902.65 ± 0.02 km, and the semi-major control deviation is within 10 m, and then the phase will drift back. It can be concluded that the orbit control precision is very high, which is mainly related to the proportional coefficient of the attitude-controlled thruster. Inaccurate calibration of this coefficient will affect the orbit control accuracy. It proves the validity and feasibility of the whole process from satellite phase tracking to the autonomous determination of orbit control strategy, and then to orbit control. Moreover, autonomous phase maintenance is realized

(3) Figures 7 and 8 show the attitude angle and quaternion deviation curves under two control strategies. Attitude adjustment and stability are successfully realized through both attitude control algorithms. As shown in Figure 5, the attitude adjustment is completed in 200 s, the phase exceeds the threshold at 705 s, and the chemical propulsion system begins to work to ensure the attitude stability. In Figures 8(a) and 8(b), the quaternion deviation under neural network sliding mode control is within -2×10^{-3} and 2×10^{-3} in the course of orbit control, while the quaternion deviation under PD control is within -4×10^{-3} and 4×10^{-3}. Accordingly, the attitude control precision is significantly improved

(4) Figures 9(a) and 9(b) show the control torques in the orbit control process. The control torques of the neural network and PD algorithms are stabilized within 0.15 Nm and 0.5 Nm, respectively. Output torques generated by the propulsion system are shown in Figures 10(a) and 10(b); the maximum torques of the neural network and PD control are

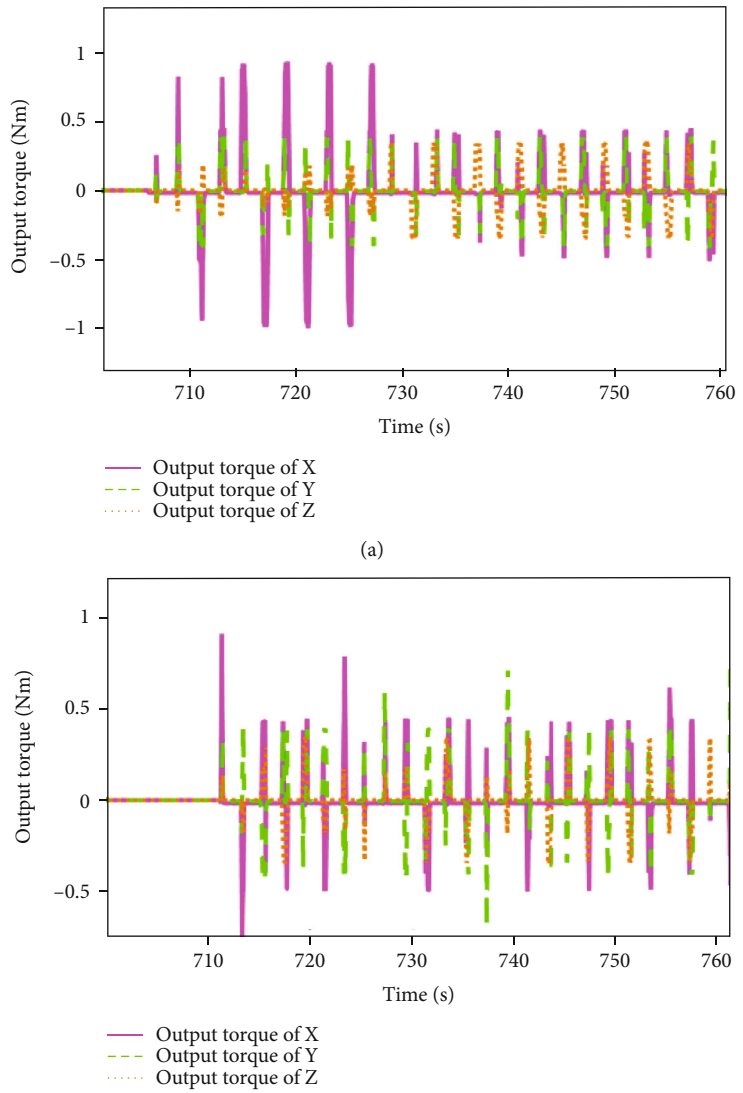

Figure 10: Output torque of propulsion system. (a) PD control. (b) Neural network sliding mode control.

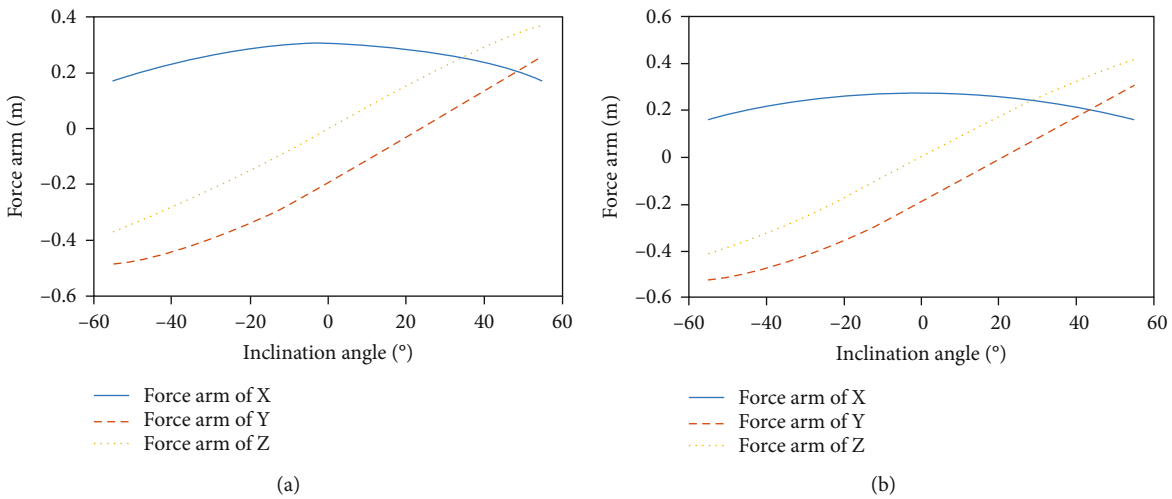

Figure 11: (a) Initial force arm. (b) Final force arm.

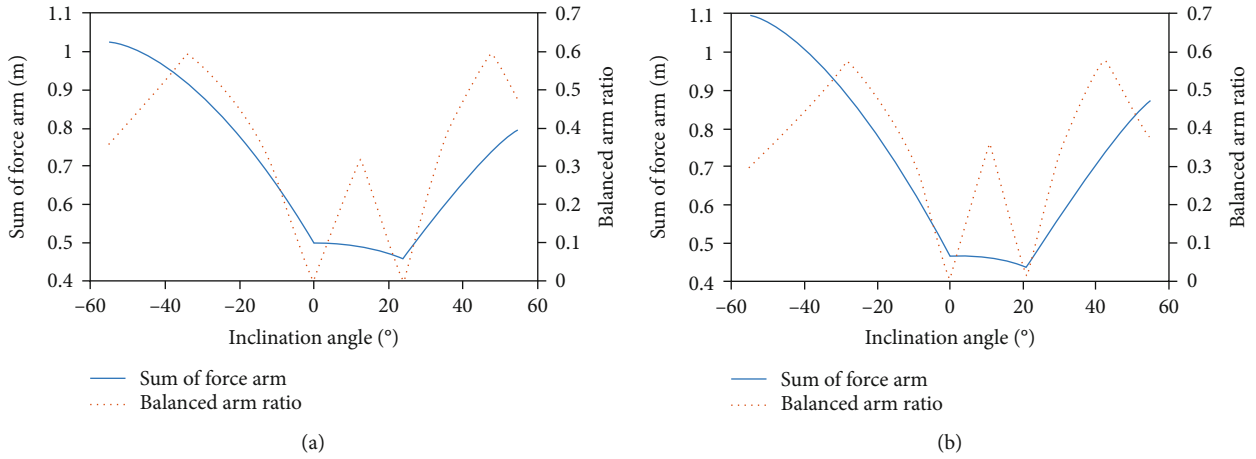

Figure 12: (a) The balanced force arm ratio alongside the ±X direction, and the sum of the initial force arm. (b) The balanced force arm ratio alongside the ±X direction, and the sum of the final force arm.

0.9 Nm, and 1.1 Nm, respectively. The designed control torque is smaller than the PD control torque. This demonstrates the superiority of the neural network control algorithm

5. Conclusions and Future Work

In this paper, a neural network-based autonomous phase control method is designed to solve the problems of configuration maintenance of remote sensing satellite constellation. Firstly, the balanced moment arm optimization method is utilized to develop the installation structure of the propulsion system to apply in the satellite. Secondly, the EKF algorithm is employed to determine the orbit used to calculate the satellite phase. Finally, an RBFNN-based attitude control method is proposed to solve the attitude disturbance problem in the course of the phase control. The effectiveness and feasibility of the proposed automatic phase control strategy of the satellite are verified through mathematical simulations.

The proposed method in this work yields the theoretical command limiting the engineering application of orbit data interaction of small satellites. If the orbit data error occurs, the orbit determination accuracy will be significantly reduced, affecting the phase maintenance. Therefore, an adaptive autonomous orbit control method is necessary to solve this problem. Although the attitude instability problem in the orbit control process should be considered for the successful realization of the orbit control, there is still a long way to achieve autonomous orbit control in orbit. To attain this goal, the reliability improvement of the orbit data in orbit and adaptive autonomous orbit control methods should be studied in the future.

Appendix

Considering the installation position and angle of the thruster on the satellite installation plate, the propulsion system's structure layout is designed using the following principles.

Principle 1: Considering the influence of thrust deviation and plume, the thruster's inclination angle is -55°~+55°. The outward and inward sides are positive and negative, respectively.

Principle 2: Considering the torque equilibrium and avoiding mutual coupling, the ratio of the maximum torque to minimum torque should be higher than 40%.

Principle 3: The inclination angle should not be too large; otherwise, the thrust loss and interference are more serious.

Principle 4: The moment arm is maximized as much as possible to save fuel consumption.

Principle 5: In order to avoid coupling torque, the geometric axis of the orbit control thruster should be installed through the center of mass as far as possible.

The inclination angle of the attitude-controlled thruster is θ_i $(i = 1, 2, 3 \cdots n)$. The distances from each thruster to the body axis are denoted by L_a, and L_b, respectively. The projected distance from each thruster to the satellite's mass center is indicated by L_c. Now, the three-axis moment arms of the satellite, L_{Xi}, L_{Yi}, and L_{Zi}, are given by

$$\begin{cases} L_{Xi} = L_a \cos(\theta_i) \\ L_{Yi} = -L_b \cos(\theta_i) + L_c \sin(\theta_i) \\ L_{Zi} = L_b \sin(\theta_i) \end{cases} \quad (A.1)$$

Now, the total moment arm L_i can be calculated as

$$L_i = |L_{Xi}|, |L_{Yi}|, |L_{Zi}| \quad (A.2)$$

The balanced arm ratio coefficient is described as

$$K_i = \min(|L_{Xi}|, |L_{Yi}|, |L_{Zi}|)/\max(|L_{Xi}|, |L_{Yi}|, |L_{Zi}|) \quad (A.3)$$

Consider that the three-axis distances are chosen as $L_a = 300$ mm, $L_b = 200$ mm, and $L_c = 450$ mm. The falling pressure working mode is adopted by the chemical propulsion system, while the mass center changes by 30 mm at

the end of the life. Therefore, there will be changes in the control torque between the former and later periods of work. As the relative moment arm is generated along the $\pm Y$ direction, the inclination control component will be generated. Thus, the installation layout along the $\pm Y$ direction is abandoned. The specific simulation analysis for the case that the inclination angle is in the $\pm X$ direction is shown in Figure 11 and Figure 12.

In Figure 11 and Figure 12, the X-axis is chosen as the installation inclination angle. Consider that the balanced force arm ratio is higher than 40%, and the force arm is maximized. According to principles (1) to (5), the installation inclination angle can be selected from -50° to -20° and from 35° to 50°. Thrust loss and orbital disturbance increase by increasing the installation inclination angle, while the onboard components' interference will be easier. As a comprehensive consideration, the installation angle is installed at -20° along the $\pm X$ direction.

Data Availability

Some or all data, models, or code generated or used during the study are proprietary or confidential in nature and may only be provided with restrictions. The specific data items and restrictions include the observation data of the global positioning system and the data of the chemical propulsion system, which are internal data in the lab, thus the data available are all provided in the paper.

Conflicts of Interest

The authors declare that there is no conflict of interest regarding the publication of this paper.

Acknowledgments

The authors acknowledge the assistance of JLICT Center of Characterization and Analysis. Xin Wang and Guogang Wang would like to acknowledge the technical support from JLICT CCA. This research is supported by the Startup Project of Doctor Scientific Research (2020013).

References

[1] T. Yamamoto, Y. Arikawa, Y. Ueda et al., "Autonomous precision orbit control considering observation planning: ALOS-2 flight results," *Journal of Guidance, Control, and Dynamics*, vol. 39, no. 6, pp. 1244–1264, 2016.

[2] L. J. Xu, Y. Hu, and T. T. Jiang, "Autonomous rendezvous control and determination of unknown target orbit," *IFAC Proceedings*, vol. 47, no. 3, pp. 9709–9714, 2014.

[3] X. W. Wang, G. Song, R. Leus, and C. Han, "Robust earth observation satellite scheduling with uncertainty of cloud coverage," *IEEE Transactions on Aerospace and Electronic Systems*, vol. 56, no. 3, pp. 2450–2461, 2020.

[4] S. Peng, H. Chen, C. Du, J. Li, and N. Jing, "Onboard observation task planning for an autonomous earth observation satellite using long short-term memory," *IEEE Access*, vol. 6, pp. 65118–65129, 2018.

[5] M. P. Clarizia and C. S. Ruf, "Wind speed retrieval algorithm for the cyclone global navigation satellite system (CYGNSS) mission," *IEEE Transactions on Geoscience and Remote Sensing*, vol. 54, no. 8, pp. 4419–4432, 2016.

[6] Y. X. Yang, Y. Y. Li, J. L. Li, and C. Yang, "Progress and performance evaluation of BeiDou global navigation satellite system: data analysis based on BDS-3 demonstration system," *Science China-earth Sciences*, vol. 61, no. 5, pp. 614–624, 2018.

[7] M. D. Sanctis, E. Cianca, G. Araniti, I. Bisio, and R. Prasad, "Satellite communications supporting internet of remote things," *IEEE Internet of Things Journal*, vol. 3, no. 1, pp. 113–123, 2016.

[8] F. A. Fernandez, "Inter-satellite ranging and inter-satellite communication links for enhancing GNSS satellite broadcast navigation data," *Advances in Space Research*, vol. 47, no. 5, pp. 786–801, 2011.

[9] H. J. Konigsmann, J. Collins, S. Dawson, and J. R. Wertz, "Autonomous orbit maintenance system," *Acta Astronautica*, vol. 39, no. 9-12, pp. 977–985, 1996.

[10] Y. Plam, R. E. Allen, J. R. Wertz, and T. Bauer, "Autonomous orbit control experience on TacSat-2 using microcosm's orbit control kit (OCK)," in *31st Annual AAS Guidance and Control Conference*, Breckenridge, Colorado, 2008.

[11] G. Gaias and J. Ardaens, "Flight demonstration of autonomous noncooperative rendezvous in low earth orbit," *Journal of Guidance, Control, and Dynamics*, vol. 41, no. 6, pp. 1337–1354, 2018.

[12] A. Christian, D. A. Simone, and E. Michael, "Precise ground-in-the-loop orbit control for low earth observation satellites," *Proceedings of the 18th International Symposium on Space Flight Dynamics*, vol. 548, pp. 333–338, 2004.

[13] H. Bolandi and S. Abrehdari, "Precise autonomous orbit maintenance of a low earth orbit satellite," *Journal of Aerospace Engineering*, vol. 31, no. 4, article 04018034, 2018.

[14] S. D. Florio, S. D. Amico, and G. Radice, "Precise autonomous orbit control in low earth orbit," in *AIAA/AAS Astrodynamics Specialist Conference*, p. 4811, Minneapolis, Minnesota, 2012.

[15] A. Garulli, A. Giannitrapani, M. Leomanni, and F. Scortecci, "Autonomous low-earth-orbit station-keeping with electric propulsion," *Journal of Guidance, Control, and Dynamics*, vol. 34, no. 6, pp. 1683–1693, 2011.

[16] S. De Florio, S. Damico, and G. Radice, "Virtual formation method for precise autonomous absolute orbit control," *Journal of Guidance, Control, and Dynamics*, vol. 37, no. 2, pp. 425–438, 2014.

[17] W. C. Zhong and P. Gurfil, "Mean orbital elements estimation for autonomous satellite guidance and orbit control," *Journal of Guidance, Control, and Dynamics*, vol. 36, no. 6, pp. 1624–1641, 2013.

[18] M. Z. Li and B. Xu, "Autonomous orbit and attitude determination for Earth satellites using images of regular-shaped ground objects," *Aerospace Science and Technology*, vol. 80, pp. 192–202, 2018.

[19] G. Zhai, Y. Y. Li, and X. Z. Bi, "Conservative term constrained kalman filter for autonomous orbit determination," *IEEE Transactions on Aerospace and Electronic Systems*, vol. 54, no. 2, pp. 783–793, 2018.

[20] Y. Jiang, S. J. Ma, Y. Wang, and W. Zhao, "Reduced-dynamic EKF-based GPS+BDS real-time orbit determination. International Conference Signal and Information Processing," *In International Conference On Signal And Information*

Processing, Networking And Computers, vol. 494, 2019, pp. 120–127, Springer, Singapore, 2019.

[21] M. Bagci and C. Hajiyev, "Integrated NRM/EKF for LEO satellite GPS based orbit determination," in *IEEE International Workshop on Metrology for Aerospace (MetroAeroSpace)*, pp. 462–467, Florence, Italy, 2016.

[22] X. C. Sun, P. Chen, C. Macabiau, and C. Han, "Autonomous orbit determination via kalman filtering of gravity gradients," *IEEE Transactions on Aerospace and Electronic Systems*, vol. 52, no. 5, pp. 2436–2451, 2016.

[23] Y. Sato, S. Fujita, T. Kuwahara et al., "Design and evaluation of thruster control approach for mi-cro-satellite ALE-2," in *IEEE/SICE International Symposium on System Integration*, Honolulu, HI, USA, 2020.

[24] Y. Gao, Z. You, and B. Xu, "Integrated design of autonomous orbit determination and orbit control for GEO satellite based on neural network," *International Journal of Aerospace Engineering*, vol. 2020, 13 pages, 2020.

[25] D. Bock and M. Tajmar, "Highly miniaturized FEEP propulsion system (NanoFEEP) for attitude and orbit control of CubeSats," *Acta Astronautica*, vol. 144, pp. 422–428, 2018.

[26] H. Yang and J. K. Liu, "An adaptive RBF neural network control method for a class of nonlinear systems," *IEEE/CAA Journal of Automatica Sinica*, vol. 5, no. 2, pp. 457–462, 2018.

[27] C. H. Cheng and S. L. Shu, "Application of GA-based neural network for attitude control of a satellite," *Aerospace Science and Technology*, vol. 14, no. 4, pp. 241–249, 2010.

[28] S. Jung, "Improvement of tracking control of a sliding mode controller for robot manipulators by a neural network," *International Journal of Control, Automation and Systems*, vol. 16, no. 2, pp. 937–943, 2018.

[29] D. Asadi and S. A. Bagherzadeh, "Nonlinear adaptive sliding mode tracking control of an airplane with wing damage," *Journal of Aerospace Engineering*, vol. 232, no. 8, pp. 1405–1420, 2018.

[30] D. K. Giri, "Fast finite-time sliding mode magnetic attitude control of satellites," *AIAA Scitech 2019 Forum*, San Diego, California, 2019.

[31] R. W. Zhang, *Satellite Orbit and Attitude Dynamics and Control*, Beijing: Beijing university of aeronautics and astronautics press, Beijing, China, 1998.